Three-dimensional structure of buried heterointerfaces revealed by multislice ptychography

Colum M. O'Leary,[1,†] Haozhi Sha,[1,†] Jianhua Zhang,[2,†] Cong Su,[3,4,5] Salman Kahn,[3,4,5] Huaidong Jiang,[2] Alex Zettl,[3,4,5] Jim Ciston,[6] and Jianwei Miao[1,*]

[1] *Department of Physics & Astronomy and California NanoSystems Institute, University of California, Los Angeles, California 90095, USA*

[2] *School of Physical Science and Technology, ShanghaiTech University, Shanghai 201210, China*

[3] *Department of Physics, University of California at Berkeley, Berkeley, California 94720, USA*

[4] *Materials Sciences Division, Lawrence Berkeley National Laboratory, Berkeley, California 94720, USA*

[5] *Kavli Energy NanoSciences Institute at the University of California, Berkeley, California 94720, USA*

[6] *National Center for Electron Microscopy Facility, Molecular Foundry, Lawrence Berkeley National Laboratory, Berkeley, California 94720, USA*

(Received 29 August 2023; revised 1 June 2024; accepted 10 June 2024; published 8 July 2024)

We report on the three-dimensional (3D) structure determination of a twisted hexagonal boron nitride (h-BN) heterointerface from a single-view dataset using multislice ptychography. We identify the buried heterointerface between two twisted h-BN flakes with a lateral resolution of 0.57 Å and a depth resolution of 2.5 nm. The latter represents a significant improvement (∼2.7 times) over the aperture-limited depth resolution of incoherent imaging modes, such as annular-dark-field scanning transmission electron microscopy. This improvement is attributed to the diffraction signal extending beyond the aperture edge, with the depth resolution set by the curvature of the Ewald sphere. Future advancements in this approach could enhance the depth resolution to the subnanometer level and enable the identification of individual dopants, defects, and color centers in twisted heterointerfaces and other materials.

DOI: 10.1103/PhysRevApplied.22.014016

I. INTRODUCTION

The development of twisted van der Waals (vdW) heterostructures, where individual layers of two-dimensional (2D) materials are successively stacked at relative rotation angles, has led to exciting applications in optoelectronics, sensing, energy storage, quantum computing, and more [1,2]. The heterointerfaces in these materials are hosts of several exotic properties and phenomena such as unique band gaps [3,4], superconducting behavior [5,6], and confined photon emission [7,8]. While aberration-corrected electron microscopy can routinely image 2D materials at subangstrom resolution [9], it remains a challenge for high-resolution 3D imaging of buried heterointerfaces. Currently, the highest-resolution 3D imaging method is atomic electron tomography (AET) [10,11], which acquires a tilt series of projections from a sample by annular dark-field (ADF)-scanning transmission electron microscopy (STEM) and uses powerful algorithms to reconstruct the 3D structure of the sample. The 3D positions of individual atoms can then be localized with high precision [12]. AET has been advanced to determine the 3D atomic structure of crystal defects and amorphous materials [13–17]. However, current AET workflows rely on obtaining a number of ADF-STEM images at different sample orientations, which offers weak signals of the light elements (i.e., B, C, and N) abundant in 2D materials. While ptychographic AET (pAET) has recently been proposed to resolve the 3D atomic positions of low-Z elements [18], the experimental implementation of the method is still in its infancy [19]. The second 3D imaging approach is based on the principle of confocal microscopy, in which ADF-STEM is used to acquire a focal series from a single angle to reveal a 3D structure with a depth resolution of several nanometers [20–23]. The depth resolution is limited by the convergence semiangle subtended by the probe-forming aperture and is typically 1–2 orders of magnitude lower than the corresponding lateral resolutions [20–23]. The third approach is based on the principle of ankylography [24], a coherent diffractive imaging method [25], which requires neither tilting of the sample nor scanning of the focus position. Although it was controversial when ankylography was first published [26,27], this method of 3D structure determination from a single view has since inspired the development of multislice ptychography

*Contact author: j.miao@ucla.edu, miao@physics.ucla.edu
†These authors contributed equally to this work.

(MSP) [28–30] and other approaches using electrons, x-rays, and visible light [31–38]. In this Paper, we advance MSP to determine the 3D structure of a buried heterointerface of two large, twisted h-BN crystals from a single-view dataset, with lateral and depth resolutions of 0.57 Å and 2.5 nm, respectively. Furthermore, we observe a depth resolution dependence on the maximum diffraction angle subtended by the detector, which is in accordance with ankylography [24].

II. MULTISLICE PTYCHOGRAPHY WORKFLOW

Figure 1 shows a schematic of the experimental setup for MSP on twisted h-BN crystals, in which a focused probe is scanned in a raster across the sample and 2D diffraction patterns are collected by a fast pixelated detector. The resulting data acquired from the scan comprises a single-view four-dimensional ptychographic array, which is used as input to an iterative phase retrieval algorithm [25,39,40]. Unlike typical STEM imaging techniques such as bright-field, annular bright- or dark-field, and differential phase contrast, the ptychographic reconstruction utilizes both the bright-field signal that extends to the semiconvergence angle (α), as well as the dark-field signal up to the maximum collection angle (θ) [41,42]. Furthermore, the reconstruction incorporates the inverse multislice approach for overcoming dynamical scattering from thick samples [28–30]. The output of the algorithm is the complex transmission function of the object for each slice of the specimen, as well as the complex function of the probe, which can be decomposed into several orthogonal modes to account for partial coherence effects [43–45]. The phase of the transmission function is highly sensitive to slight disturbances in the electron wave, and can be plotted to generate high-fidelity reconstructions of light-element species [46,47] with significantly higher light-element contrast than ADF-STEM imaging. In recent studies, MSP has been used to reveal structural inhomogeneities in single crystals [30,48,49] and distinguish individual nanotubes in projection [29,50,51]. Here, we demonstrate the application of MSP to stacked 2D materials. As shown in Fig. 1, upon MSP reconstruction, the top (ψ_{top}) and bottom (ψ_{bot}) crystals in the twisted system can be visualized independently, while a separate phase slice can be determined for the interface (ψ_{int}).

To demonstrate the application of MSP to vdW heterointerfaces, we performed a ptychographic experiment on two twisted h-BN flakes [7] deposited onto a holey Si grid, as shown in Fig. 2(a). The experimental data was collected using the TEAM I double-corrected (S)TEM instrument at the National Center for Electron Microscopy, installed with a Gatan K3 pixelated detector. In contrast to many

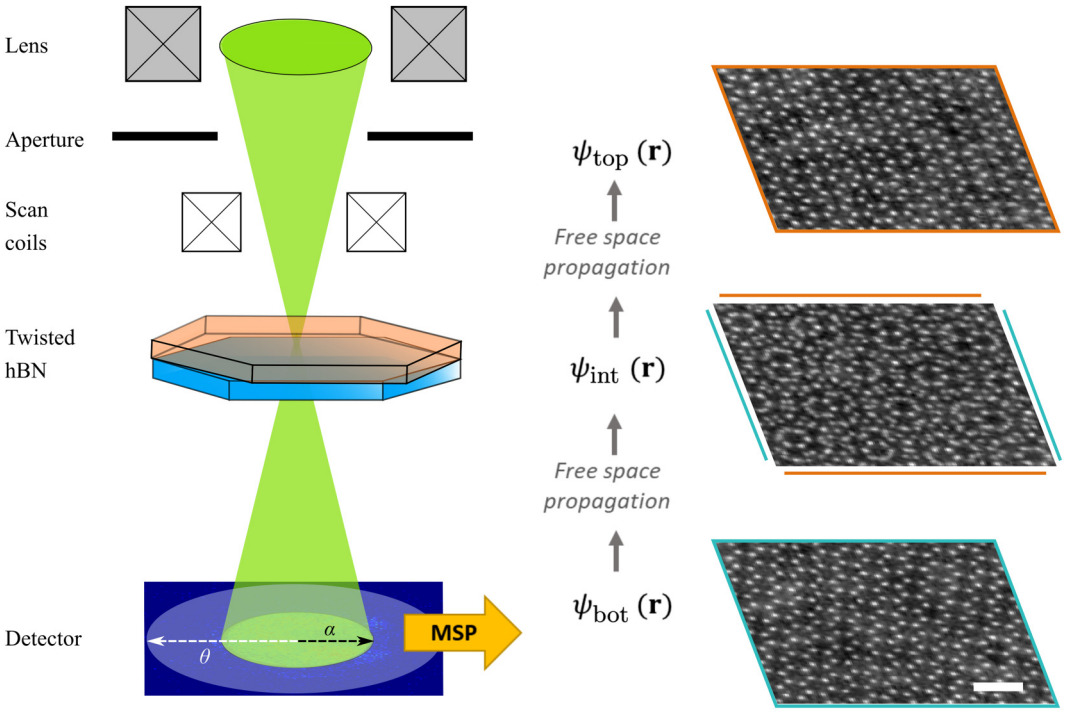

FIG. 1. Schematic of multislice ptychography (MSP) on twisted h-BN crystals. At each point in a raster scan across the sample, a diffraction pattern is collected by a fast pixelated detector. The bright-field signal collected by the detector is highlighted in green with convergence semiangle α, while the dark-field signal comprises the annulus shaded in pale blue with maximum diffraction angle θ. Reconstruction via MSP provides atomic-scale phase reconstructions of different sample slices, revealing nanoscale depth information. Here, each phase slice shown is generated from the sum of seven separate 0.5-nm slices. Scale bar: 0.5 nm.

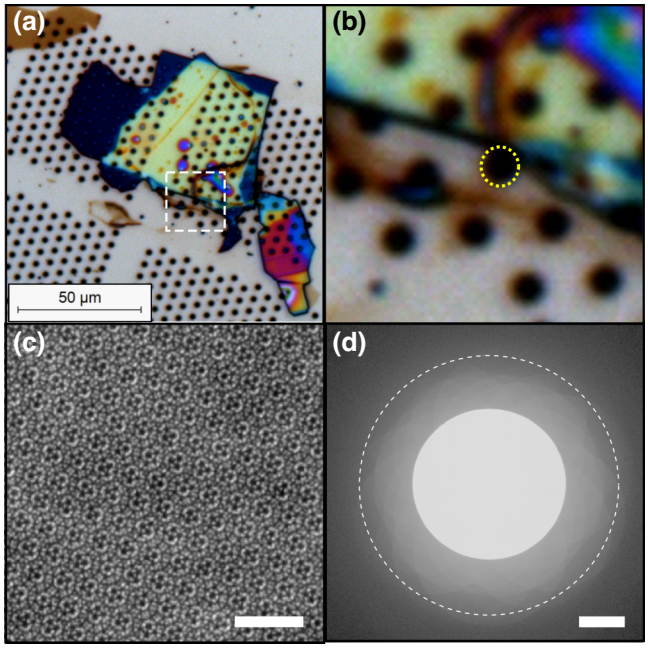

FIG. 2. Conventional imaging of twisted h-BN crystals. (a) Optical microscope image of twisted h-BN flakes. (b) A magnified view of the region enclosed by the white square in (a) shows two twisted flakes. The dashed circle indicates the grid hole used for data collection. (c) Annular dark-field (ADF) image of the twisted h-BN flakes. Scale bar: 2 nm. (d) Averaged diffraction pattern (logarithmic scale) from the ptychographic dataset, where the maximum diffraction angle is 36.2 mrad. Scale bar: 10 mrad.

electron microscopy studies on 2D materials systems, an acceleration voltage of 300 kV was used for this experiment to improve the depth resolution of the ptychographic reconstruction. A convergence semiangle of 17.1 mrad was used to mitigate the partial coherence effects of the instrument while maintaining subangstrom lateral resolution capabilities. A total of 256×256 diffraction patterns (512×512 px, with a dwell time of 0.87 ms) were acquired with a step size of 0.25 Å between adjacent scan positions, resulting in a cumulative electron dose of 4.5×10^6 e^- $Å^{-2}$. The data was collected over one of the holes in the sample grid to minimize background intensity, as highlighted with the dashed circle in Fig. 2(b). An ADF image acquired over the crystal structure, displayed in Fig. 2(c), clearly shows the atomic columns of both crystals. Furthermore, the averaged diffraction pattern displayed in Fig. 2(d) shows several diffraction disks interfering with the zeroth-order disk, indicating that both crystal flakes in the twisted h-BN are contributing to the diffraction intensity measurements. The relative in-plane twist angle θ_t between the crystals was determined as 19.05° from the Fourier transform of seven interface slices [i.e., from ψ_{int} in Fig. 1]. In recent studies, highly twisted h-BN interfaces ($\theta_t > 14°$) have demonstrated strong photon emission in the UV regime indicative of the presence of nitrogen color centers; thus, the capability to decipher the location of highly twisted interfaces is of notable importance for quantum sensing and computing applications [7]. The direct correlation between sites of photon emission and the location of nitrogen vacancies is beyond the scope of this work; this will be examined in future studies.

The ptychographic reconstructions were performed using the maximum-likelihood multislice engines available in the FOLD-SLICE package, which has been adapted from the PTYCHOSHELVES package [30,52,53]. A 128×128 scan region was chosen from the original dataset, and the detector was binned to 128×128 pixels before performing the reconstruction. Next, the complex object function was calculated using two separate reconstruction runs: (1) a single-slice ptychography reconstruction and (2) an MSP reconstruction incorporating 34 object slices. In addition, the probe was decomposed into eight orthogonal modes for each reconstruction run. The reconstruction pixel size, Δr, was set as 0.0218 nm by padding the diffraction patterns to 160×160 pixels, and a slice

TABLE I. Reconstruction parameters for the single- and multislice ptychography reconstructions performed using the fold-slice package.

Reconstruction	Max. likelihood, single-slice	Max. likelihood, multislice
No. of scan positions	128×128	128×128
No. of detector pixels (binned)	128×128	128×128
Max collection angle	36 mrad	36 mrad
Engine	GPU	GPU_MS
No. of probe modes	8	8
No. of iterations, round 1	100	120
No. of iterations, round 2	100	100
Noise model	Amplitude likelihood	Amplitude likelihood
beta_LSQ	0.5	0.5
delta_p	0.1	0.1
Layer regularization, round 1	N/A	0.5
No. of slices	N/A	34
Propagation distance per slice	N/A	0.5 nm
No. of reconstruction pixels, round 1	128×128	128×128
No. of reconstruction pixels, round 2	160×160	160×160
Reconstruction pixel size, round 1	0.0272 nm	0.0272 nm
Reconstruction pixel size, round 2	0.0218 nm	0.0218 nm
Overdetermination ratio (σ)	109.98	7.38

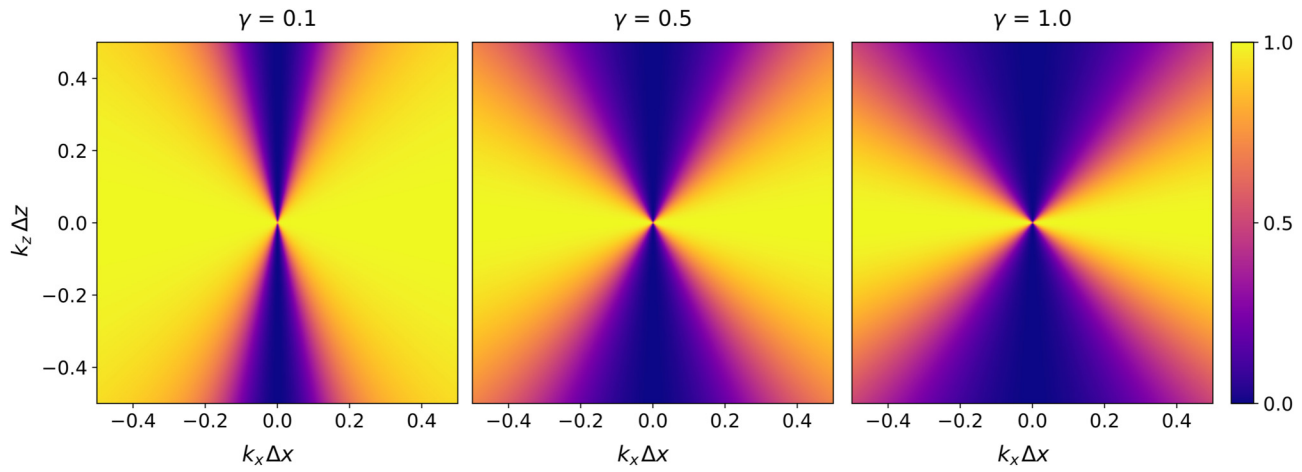

FIG. 3. Plots of the weighting functions (color scale) generated from regularization factors of $\gamma = 0.1$ (left), $\gamma = 0.5$ (middle), and $\gamma = 1.0$ (right).

spacing, Δz, of 0.5 nm was chosen in order to maximize depth resolution while minimizing the crosstalk of low spatial frequencies [54]. Table I displays the reconstruction parameters used for the single-slice and multislice reconstructions performed on the twisted h-BN sample. Each "round" corresponds to a run of the ptychographic engine with a specific set of reconstruction parameters.

For the multislice reconstruction performed in this work, the parameters are changed after 120 iterations (i.e., round 1), after which the next iteration corresponds to the first iteration of round 2. Several parameters were tuned to optimize the fidelity of the multislice reconstruction. For example, a 3D weighting function, W, was applied to the object in reciprocal space to mitigate artifacts caused by the crosstalk of low spatial frequencies between adjacent reconstruction slices [30,54]. This function is expressed as follows:

$$W = 1 - \left(\tan^{-1}\left(\left[\gamma\frac{k_z\Delta z}{k_r\Delta r + \epsilon}\right]^2\right)/(\pi/2)\right), \quad (1)$$

where k_r and k_z correspond to the spatial frequencies in the lateral and depth directions, ϵ is a small number to prevent division-by-zero errors, and γ is a regularization parameter. A visualization of W is shown for the 2D case ($k_x - k_z$) in Fig. 3. By increasing γ, the transfer of information with low in-plane frequency is dampened along the depth direction, resulting in an object reconstruction with fewer artifacts at the expense of lower depth resolution. In this work, γ was set to 0.5 (Table I). Applying values of γ below 0.5 resulted in increased artifacts in the reconstruction. In addition, a weighting factor (beta_LSQ) was applied to the optimal probe and update steps determined from the least squares method to avoid divergence [52], and a further damping term (delta_p) was applied to the object update step to ensure that small changes in input correspond to small changes in output [52]. The values of beta_LSQ and delta_p used for each reconstruction run are displayed in Table I.

III. 3D RECONSTRUCTION RESULTS

To demonstrate the improvement of lateral resolution using MSP, the phase of the object functions obtained from the single-slice and multislice reconstructions are shown in Figs. 4(a) and 4(c), respectively. The summed-multislice result here was obtained from 24 slices of the object reconstruction. It is evident that the width of the atomic column potentials is significantly reduced in the case of MSP. The MSP reconstruction reveals several atomic column potentials that could not be observed using the single-slice approach, which suggests that the dynamical scattering effects have been accounted for using the multislice approach. For further comparison, the Fourier transforms of the single- and multislice approaches are shown in Figs. 4(b) and 4(d), respectively. It is clear that the multislice approach resolves diffraction spots out to 0.57 Å, while the single-slice approach can resolve spots out to 0.72 Å. In addition, there is a noticeable improvement in the probe reconstruction using MSP. Figure 5 shows the eight complex probe mode reconstructions for the single-slice (top) and multislice (bottom) approaches. For the single-slice approach, the higher order modes are corrupted with spurious intensity peaks and significant probe broadening, which may be attributed to the dynamical scattering caused by the h-BN sample. In the case of the multislice reconstruction, however, the probe intensity is centered on the origin, and the fringes are clearly resolved in the phase of all eight modes. This improvement of MSP over single-slice ptychography is significant because, while h-BN columns would not be expected to cause significant dynamical scattering at such crystal thicknesses

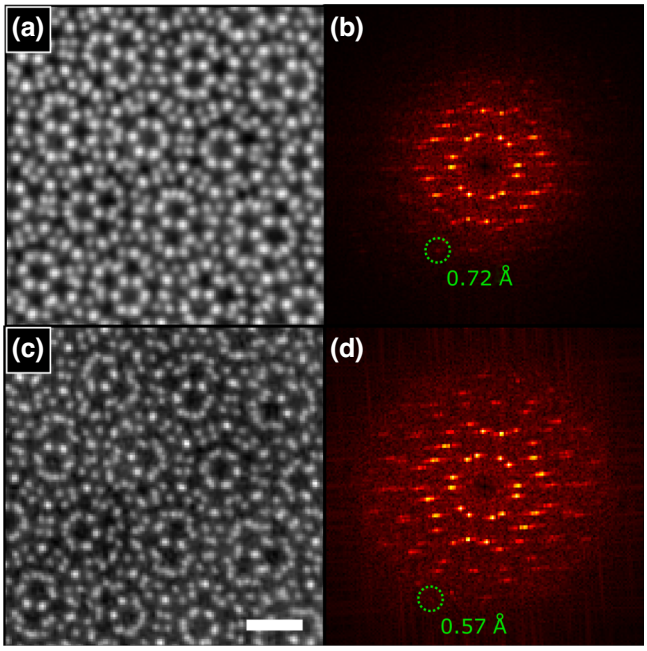

FIG. 4. Comparison of lateral resolution for single- and multislice ptychography. (a) Reconstructed object phase obtained from single-slice ptychography. (b) Magnitude of the Fourier transform of (a), showing a lateral resolution of 0.72 Å. (c) Object phase obtained from the sum of 24 0.5-nm-thick slices reconstructed via multislice ptychography. Scale bars for (a) and (c): 0.5 nm. (d) Magnitude of the Fourier transform of (c), showing a lateral resolution of 0.57 Å.

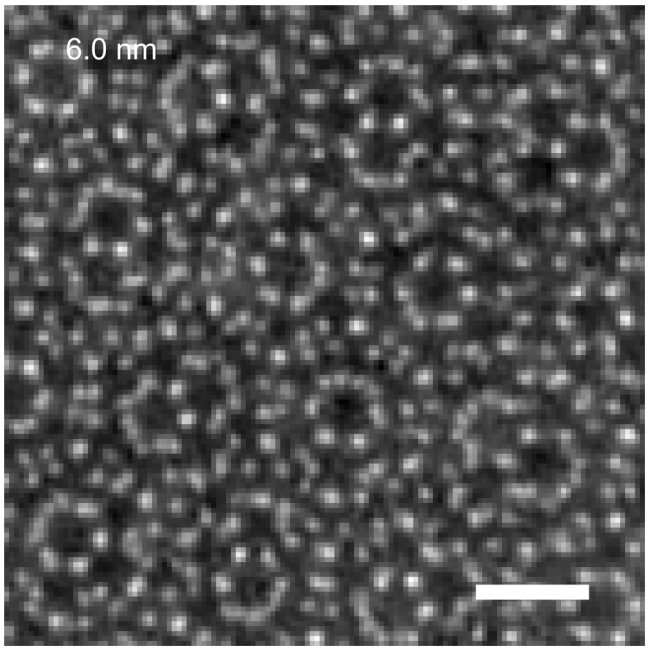

VIDEO 1. Reconstructed phase from all 34 slices of the twisted h-BN crystals. The thickness labels correspond to the depth of the slice with respect to the sample surface. Scale bar: 0.5 nm.

with 300 kV electrons, there are noticeable improvements to the reconstruction when such scattering is accounted for.

Video 1 shows the series of all 34 slices reconstructed by MSP, demonstrating the depth-dependent structural variation of the twisted h-BN crystals. The h-BN sample thickness was estimated from the reconstruction as 12 nm (24 slices), and the distance between each sample slice and the top surface of the sample is labeled for reference. To find the location of the buried interface, we analyze five 1-nm-thick slices with a depth position ranging from 4 to 8 nm below the surface of the top flake. Figure 6 displays the phase images and corresponding Fourier transforms of the five slices. The phase image of the first slice clearly shows the h-BN atomic structure of the top flake [Fig. 6(a)], while the weak Bragg peaks of the bottom flake are also visible [Fig. 6(f)]. Upon propagation toward the interface [Figs. 6(b) and 6(g)], the contrast of the real-space phase and the intensity of the Bragg peak of the bottom flake increase. At a depth position of 6 nm (i.e., the third slice), atomic columns from both flakes are clearly visible from the phase slice in Fig. 6(c), and there are similar Bragg peak contributions as shown in Fig. 6(h). Upon inspection of all 34 slices, the interface is estimated to be located 6 nm below the surface of the top h-BN flake (Video 1). After propagation through the interface to the depth position of 7 nm [Figs. 6(d) and 6(i)], the relative contribution of the bottom flake increases, while the final displayed slice only clearly shows the bottom flake in the phase image [Fig. 6(e)], with weak Bragg peaks from the top flake [Fig. 6(j)]. To further observe the depth-dependent variation of MSP, the x–z profiles of the top flake from the multislice reconstruction are displayed in Video 2. A subregion of five pixels in the y-direction, labeled with a white rectangle (left panel), is summed to calculate the depth profile (right panel) of the enclosed pixels. This subregion is scanned vertically to display depth profiles for the entire field of view. When the subregion scans over a row of atomic columns, doublet peaks are clearly observed, while contributions from the bottom flake appear several nanometers below the top surface. Although the transition from the top flake to the bottom flake can be clearly observed in Video 2, the absence of structural inhomogeneities within the crystal is a result of insufficient resolution in the depth direction. In the next section, we describe the procedure used to estimate the depth resolution for the h-BN experiment.

IV. DEPTH RESOLUTION DETERMINATION

The depth resolution of the MSP reconstruction is estimated based on a knife-edge analysis. First, the coordinates of the atomic columns for the top flake are determined using the peak fitting functions of the ABSOLUTE INTEGRATOR package in MATLAB [55]. In

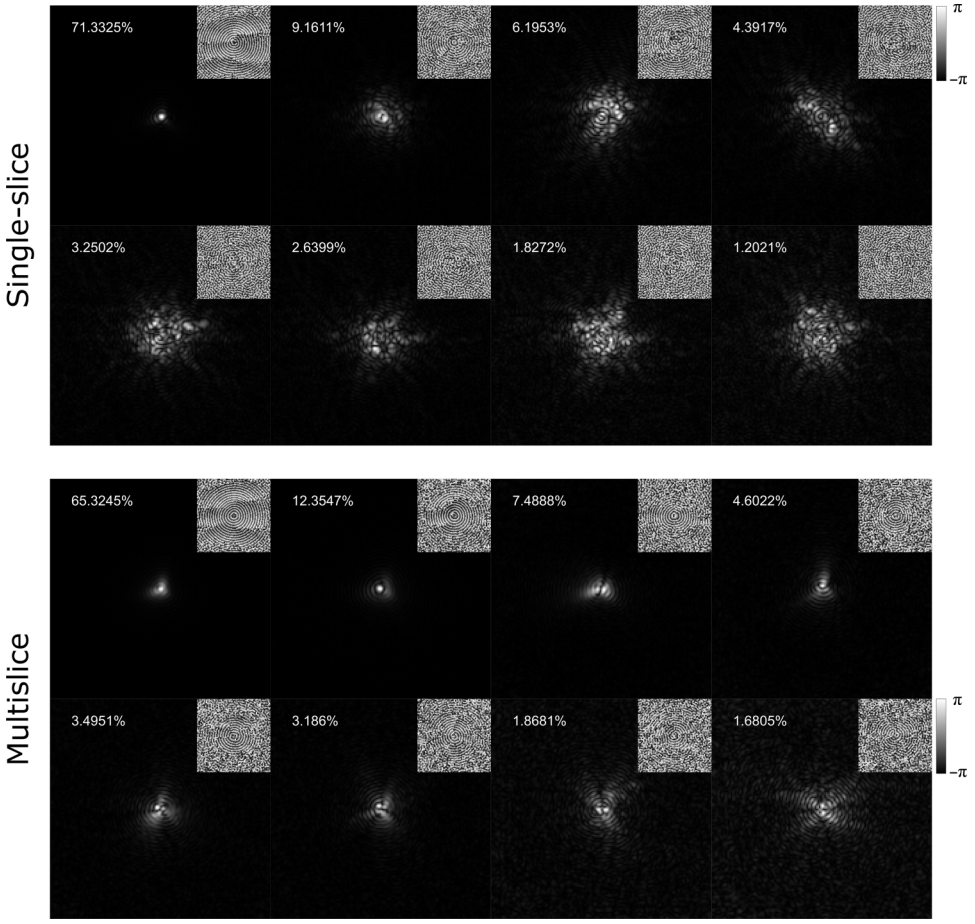

FIG. 5. Complex amplitude (main) and phase (inset) of the eight reconstructed probe modes from single- (top) and multislice (bottom) ptychography. The relative intensity weights of each probe mode are labeled for each panel. Scale bar: 0.5 nm. Color bar scale: phase (radians).

order to determine the area of each column peak, a sum of the reconstructed slices of the top flake (i.e., ψ_{top} in Fig. 1) is used as a basis for masking. The mask is applied to each phase slice and, for each atomic coordinate, the phase within the surrounding mask is summed and registered as a function of thickness. The average phase thickness profile is determined from 100 individual atomic columns, and the normalized result of a representative column is plotted

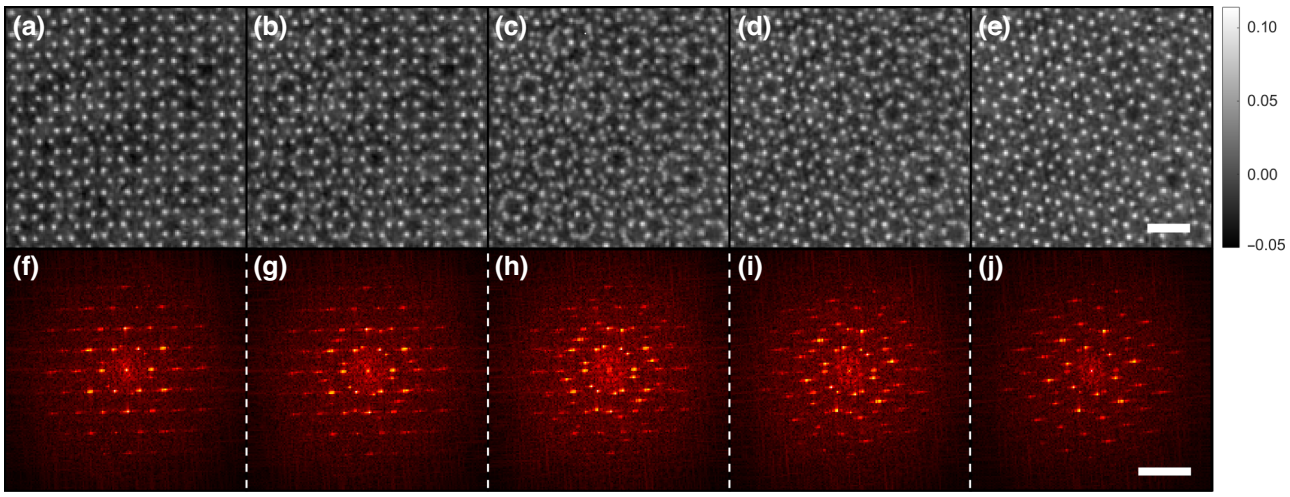

FIG. 6. Probing a buried interface in the twisted h-BN flakes. Reconstructed phase slices of the twisted h-BN flakes at depth positions of (a) 4 nm, (b) 5 nm, (c) 6 nm, (d) 7 nm, and (e) 8 nm below the surface of the top flake. Scale bar: 0.5 nm. (f)–(j) Magnitude of the Fourier transforms of the corresponding five-phase images. Scale bar: 10 nm^{-1}. Color bar scale: phase (radians).

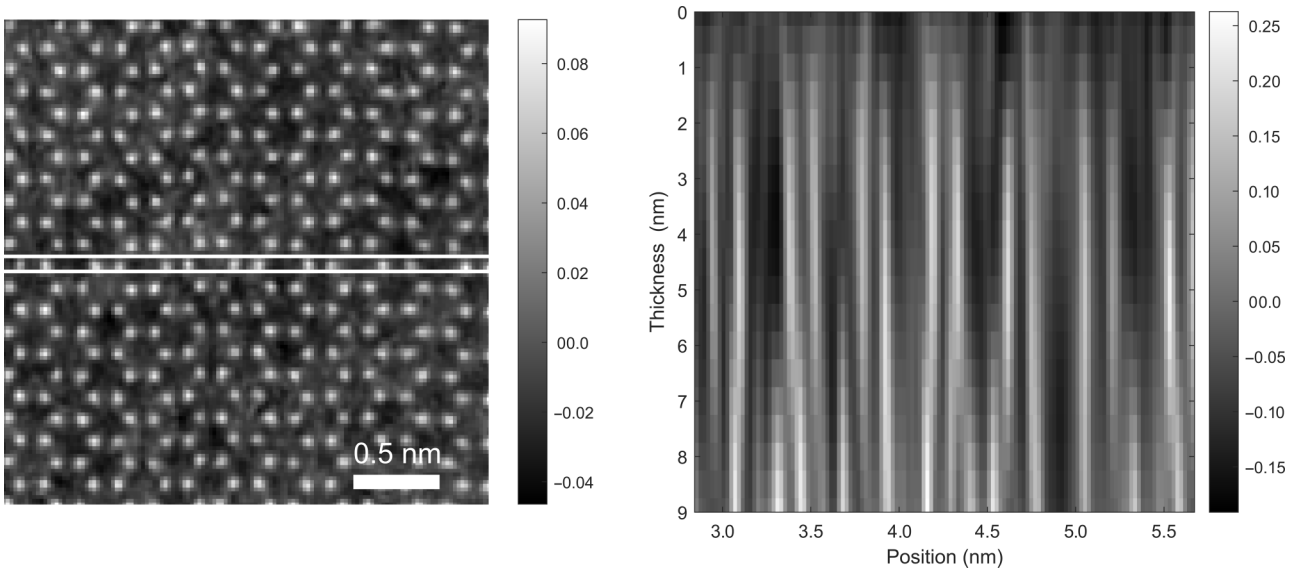

VIDEO 2. x–z phase profile (right) of the atomic columns in the top flake (left) calculated from the scanned subregion (white rectangle).

in Fig. 7(a). The reconstructed phase slices i–iv shown in Fig. 7(b) highlight the propagation of the peak phase intensity from the vacuum above the sample into the top flake. Using linear interpolation of the scatter plot, the knife-edge resolution is obtained by calculating the difference between the thickness values at 10% and 90% maximum phase. The average depth resolution based on the 100 columns is determined to be 2.5 nm. This is consistent with previous numerical simulation results [30] and is 2.7 times higher than the aperture-limited depth resolution of 6.7 nm, calculated via $d_z \approx \lambda/\alpha^2$, where d_z is the depth resolution, λ is the wavelength, and α is the convergence semiangle (Fig. 1). We attribute the significant resolution improvement to the diffraction signal beyond the bright-field disk. According to ankylography [24], the depth resolution is determined by

$$d_z \approx \frac{2\lambda}{\theta^2} \tag{2}$$

where θ is the maximum diffraction angle (Fig. 1) and the factor of 2 arises because it is derived from coherent diffraction with an assumed parallel incident beam. In our experimental data, the maximum diffraction angle is 36.2 mrad [Fig. 2(d)], which corresponds to a depth resolution of 3 nm and is more consistent with our depth-resolution measurement of 2.5 nm. The slightly improved measured depth resolution is due to the parallel incident beam assumption in Eq. (2). If we consider the convergence semiangle in the experiment, the maximum diffraction angle of some signals is actually larger than 36.2 mrad. To observe the improvement of depth resolution with maximum diffraction angle, the average knife-edge resolution was plotted for four separate reconstructions with different angular cutoff values [Fig. 7(c)]. The calculated resolution and standard deviation (error bars) decrease for larger cutoff angles up to the maximum diffraction angle of 36.2 mrad. Upon padding the diffraction patterns to 45.2 mrad before reconstruction, the variance of the resolution further decreases but the mean resolution does not improve. It should be noted that the improvement of the depth resolution requires the increase of the probe overlap and/or the oversampling of the diffraction patterns so that the number of independently measured points is larger than that of the unknown variables [56]. This *overdetermination ratio* is calculated by taking the ratio between known and unknown variables in the dataset. For the experimental h-BN dataset shown here, the known variables are taken as the number of nonzero pixels in the four-dimensional dataset (i.e., 77 819 054), while the unknown variables comprise a real and imaginary value for each pixel in the reconstructed object (386 × 386 pixels per slice) and probe (160 × 160 pixels per mode). Accounting for the 34 object slices and 8 probe modes, the overdetermination ratio σ_{MS} (also known as the *redundancy*) for the multislice reconstruction is calculated via

$$\sigma_{\mathrm{MS}} = \frac{77819054}{2 \times (34 \times 386^2 + 8 \times 160^2)} = 7.38, \tag{3}$$

and, for the single-slice reconstruction, σ_{SS} is calculated as follows:

$$\sigma_{\mathrm{SS}} = \frac{77819054}{2 \times (386^2 + 8 \times 160^2)} = 109.98. \tag{4}$$

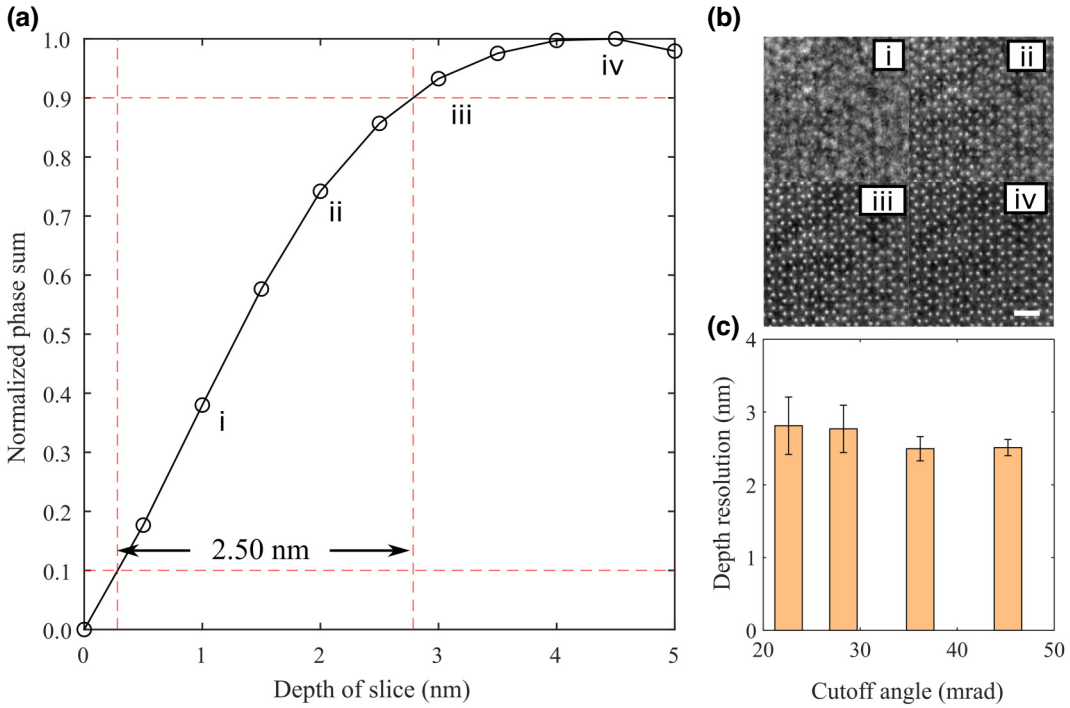

FIG. 7. Knife-edge plot for the twisted h-BN crystals. (a) Representative knife edge for an atomic column in the top h-BN flake. A linear interpolation is applied to the measured values to calculate the knife-edge resolution corresponding to the z-distance between 10% and 90% maximum phase. (b) Reconstructed phase slices at the corresponding thickness values labeled on the knife-edge plot. Scale bar: 0.5 nm. (c) Average depth resolution as a function of angular cutoff used in the reconstruction. The measured depth resolution is 2.81 ± 0.79 nm, 2.77 ± 0.65 nm, 2.5 ± 0.33 nm, and 2.51 ± 0.22 nm for a maximum cutoff angle of 22.6, 28.3, 36.2, and 45.2 mrad, respectively.

It is expected that a larger σ will provide an improved diffraction-dependent resolution [Fig. 7(c)] converging to that expected from Eq. (2).

V. DISCUSSION AND CONCLUSIONS

Although MSP can overcome challenges imposed by most atomic-resolution (S)TEM techniques, there are several limitations to this approach. First, while MSP can provide depths of field beyond those of incoherent imaging techniques such as ADF-STEM, there is a limit to the maximum thickness (i.e., < 100 nm) that can be used as a result of significant electron absorption and dynamical scattering [30,49]. Nevertheless, we anticipate that the workflow shown here can be used to identify interfaces in light-element vdW heterostructures with cumulative thicknesses up to 50 nm. Second, as the number of slices increases, σ decreases and the mixing of low spatial frequencies between adjacent slices is significant, eventually leading to an ill-posed problem with many unknown variables. This is compounded by the coincidence loss suffered by detectors that operate via electron counting, particularly at large beam currents, as was the case for the h-BN experiment. Thus, the use of a strong regularization to symmetrize adjacent slices is crucial for increasing the fidelity of each phase reconstruction slice and improving the convergence of the algorithm. However, once the regularization is weakened for improved depth resolution, the crosstalk of low spatial frequencies may give rise to spurious intensity values, thus limiting the phase sensitivity of this approach for single-atom identification. Potential techniques to overcome this issue include using pixelated detectors with high dynamic range, acquiring several ptychographic datasets from a range of geometric aberration values to aid convergence, and performing data acquisition over a range of projection angles.

In summary, we have demonstrated the use of multislice ptychography for probing interfaces of twisted crystals on the nanoscale from a single view. The depth-resolution improvement over the aperture limit demonstrates the potential to probe crystals in projection at the subnanometer level. With further depth-resolution improvement, either via increased convergence and diffraction angles using state-of-the-art aberration correctors [57] or through tomographic methods [19,58], structural inhomogeneities at the subnanometer level should be achievable, providing important insights into the crystal order or disorder of complex 2D materials.

ACKNOWLEDGMENTS

This research was primarily supported by the U.S. Department of Energy, Office of Science, Basic Energy Sciences, Division of Materials Sciences and Engineering under Award No. DE-SC0010378. C.M.O. and H.S. acknowledge support by STROBE: a National Science Foundation Science and Technology Center under Grant No. DMR-1548924 and the Army Research Office Multidisciplinary University Research Initiative (MURI) program under Grant No. W911NF-18-1-0431. The electron microscopy experiments were performed at the Molecular Foundry, which is supported by the Office of Science, Office of Basic Energy Sciences of the U.S. Department of Energy under Award No. DE-AC02-05CH11231. C.S. and A.Z. acknowledge the support by the Director, Office of Science, Office of Basic Energy Sciences, Materials Sciences and Engineering Division, of the U.S. Department of Energy under Award No. DEAC02-05-CH11231, within the sp2 -Bonded Materials Program (KC-2207), which provided for preliminary TEM and Raman characterization of the h-BN material, and by the van der Waals Heterostructures program (KCWF16), which provided for assembly of the twisted h-BN material. Data processing was carried out using the cSAXS ptychography MATLAB package developed by the Science IT and the coherent X-ray scattering (CXS) groups, Paul Scherrer Institut, Switzerland.

[1] A. K. Geim and I. V. Grigorieva, Van der Waals heterostructures, Nature **499**, 419 (2013).

[2] Z. Hennighausen and S. Kar, Twistronics: a turning point in 2D quantum materials, Electron. Struct. **3**, 014004 (2021).

[3] X. Tian, X. Yan, G. Varnavides, Y. Yuan, D. S. Kim, C. J. Ciccarino, P. Anikeeva, M. Y. Li, N. J. Li, P. Narang, *et al.*, Capturing 3D atomic defects and phonon localization at the 2D heterostructure interface, Sci. Adv. **7**, eabi6699 (2021).

[4] V. Zatko, S. M. Dubois, F. Godel, C. Carrétéro, A. Sander, S. Collin, M. Galbiati, J. Peiro, F. Panciera, G. Patriarche, *et al.*, Band-gap landscape engineering in large-scale 2d semiconductor van der Waals heterostructures, ACS Nano **15**, 7279 (2021).

[5] S. Kezilebieke, M. N. Huda, V. Vaño, M. Aapro, S. C. Ganguli, O. J. Silveira, S. Głodzik, A. S. Foster, T. Ojanen, and P. Liljeroth, Topological superconductivity in a van der Waals heterostructure, Nature **588**, 424 (2020).

[6] Y. Lee, M. Martini, T. Confalone, S. Shokri, C. N. Saggau, D. Wolf, G. Gu, K. Watanabe, T. Taniguchi, D. Montemurro, *et al.*, Encapsulating high-temperature superconducting twisted van der Waals heterostructures blocks detrimental effects of disorder, Adv. Mater. **35**, 2209135 (2023).

[7] C. Su, F. Zhang, S. Kahn, B. Shevitski, J. Jiang, C. Dai, A. Ungar, J. H. Park, K. Watanabe, T. Taniguchi, *et al.*, Tuning colour centres at a twisted hexagonal boron nitride interface, Nat. Mater. **21**, 896 (2022).

[8] S. Susarla, M. H. Naik, D. D. Blach, J. Zipfel, T. Taniguchi, K. Watanabe, L. Huang, R. Ramesh, F. H. da Jornada, S. G. Louie, *et al.*, Hyperspectral imaging of exciton confinement within a moiré unit cell with a subnanometer electron probe, Science **378**, 1235 (2022).

[9] O. L. Krivanek, M. F. Chisholm, V. Nicolosi, T. J. Pennycook, G. J. Corbin, N. Dellby, M. F. Murfitt, C. S. Own, Z. S. Szilagyi, M. P. Oxley, *et al.*, Atom-by-atom structural and chemical analysis by annular dark-field electron microscopy, Nature **464**, 571 (2010).

[10] M. C. Scott, C. C. Chen, M. Mecklenburg, C. Zhu, R. Xu, P. Ercius, U. Dahmen, B. C. Regan, and J. Miao, Electron tomography at 2.4-ångström resolution, Nature **483**, 444 (2012).

[11] J. Miao, P. Ercius, and S. J. L. Billinge, Atomic electron tomography: 3D structures without crystals, Science **353**, aaf2157 (2016).

[12] R. Xu, C. C. Chen, L. Wu, M. C. Scott, W. Theis, C. Ophus, M. Bartels, Y. Yang, H. Ramezani-Dakhel, M. R. Sawaya, *et al.*, Three-dimensional coordinates of individual atoms in materials revealed by electron tomography, Nat. Mater. **14**, 1099 (2015).

[13] Y. Yang, C. C. Chen, M. C. Scott, C. Ophus, R. Xu, A. Pryor, L. Wu, F. Sun, W. Theis, J. Zhou, *et al.*, Deciphering chemical order/disorder and material properties at the single-atom level, Nature **542**, 75 (2017).

[14] J. Zhou, Yongsoo Yang, Yao Yang, D. S. Kim, A. Yuan, X. Tian, C. Ophus, F. Sun, A. K. Schmid, M. Nathanson, *et al.*, Observing crystal nucleation in four dimensions using atomic electron tomography, Nature **570**, 500 (2019).

[15] X. Tian, D. S. Kim, S. Yang, C. J. Ciccarino, Y. Gong, Yongsoo Yang, Yao Yang, B. Duschatko, Y. Yuan, P. M. Ajayan, *et al.*, Correlating the three-dimensional atomic defects and electronic properties of two-dimensional transition metal dichalcogenides, Nat. Mater. **19**, 867 (2020).

[16] Y. Yang, J. Zhou, F. Zhu, Y. Yuan, D. J. Chang, D. S. Kim, M. Pham, A. Rana, X. Tian, Y. Yao, *et al.*, Determining the three-dimensional atomic structure of an amorphous solid, Nature **592**, 60 (2021).

[17] S. Moniri, Y. Yang, J. Ding, Y. Yuan, J. Zhou, L. Yang, F. Zhu, Y. Liao, Y. Yao, L. Hu, *et al.*, Three-dimensional atomic structure and local chemical order of medium-and high-entropy nanoalloys, Nature **624**, 564 (2023).

[18] D. J. Chang, D. S. Kim, A. Rana, X. Tian, J. Zhou, P. Ercius, and J. Miao, Ptychographic atomic electron tomography: Towards three-dimensional imaging of individual light atoms in materials, Phys. Rev. B **102**, 174101 (2020).

[19] P. M. Pelz, S. M. Griffin, S. Stonemeyer, D. Popple, H. DeVyldere, P. Ercius, A. Zettl, M. C. Scott, and Colin Ophus, Solving complex nanostructures with ptychographic atomic electron tomography, Nat. Commun. **14**, 7906 (2023).

[20] K. van Benthem, A. R. Lupini, M. Kim, H. S. Baik, S. Doh, J. H. Lee, M. P. Oxley, S. D. Findlay, L. J. Allen, J. T. Luck, *et al.*, Three-dimensional imaging of individual hafnium atoms inside a semiconductor device, Appl. Phys. Lett. **87**, 034104 (2005).

[21] P. D. Nellist, E. C. Cosgriff, G. Behan, and A. I. Kirkland, Imaging modes for scanning confocal electron microscopy in a double aberration-corrected transmission electron microscope, Microsc. Microanal. **14**, 82 (2008).

[22] H. L. Xin and D. A. Muller, Aberration-corrected ADF-STEM depth sectioning and prospects for reliable 3D imaging in S/TEM, J. Electron Microsc. **58**, 157 (2009).
[23] H. Yang, J. G. Lozano, T. J. Pennycook, L. Jones, P. B. Hirsch, and P. D. Nellist, Imaging screw dislocations at atomic resolution by aberration-corrected electron optical sectioning, Nat. Commun. **6**, 7266 (2015).
[24] K. S. Raines, S. Salha, R. L. Sandberg, H. Jiang, J. A. Rodriguez, B. P. Fahimian, H. C. Kapteyn, J. Du, and J. Miao, Three-dimensional structure determination from a single view, Nature **463**, 214 (2010).
[25] J. Miao, P. Charalambous, J. Kirz, and D. Sayre, Extending the methodology of X-ray crystallography to allow imaging of micrometre-sized non-crystalline specimens, Nature **400**, 342 (1999).
[26] H. Wei, Fundamental limits of 'ankylography' due to dimensional deficiency, Nature **480**, E1 (2011).
[27] G. Wang, H. Yu, W. Cong, and A. Katsevich, Non-uniqueness and instability of 'ankylography', Nature **480**, E2 (2011).
[28] A. M. Maiden, M. J. Humphry, and J. M. Rodenburg, Ptychographic transmission microscopy in three dimensions using a multi-slice approach, J. Opt. Soc. Am. A **29**, 1606 (2012).
[29] S. Gao, P. Wang, F. Zhang, G. T. Martinez, P. D. Nellist, X. Pan, and A. I. Kirkland, Electron ptychographic microscopy for three-dimensional imaging, Nat. Commun. **8**, 163 (2017).
[30] Z. Chen, Y. Jiang, Y. T. Shao, M. E. Holtz, M. Odstrčil, M. Guizar-Sicairos, I. Hanke, S. Ganschow, D. G. Schlom, and D. A. Muller, Electron ptychography achieves atomic-resolution limits set by lattice vibrations, Science **372**, 826 (2021).
[31] D. Van Dyck, J. R. Jinschek, and F.-R. Chen, 'Big Bang' tomography as a new route to atomic-resolution electron tomography, Nature **486**, 243 (2012).
[32] A. Suzuki, S. Furutaku, K. Shimomura, K. Yamauchi, Y. Kohmura, T. Ishikawa, and Y. Takahashi, High-resolution multislice x-ray ptychography of extended thick objects, Phys. Rev. Lett. **112**, 053903 (2014).
[33] C. L. Jia, S. B. Mi, J. Barthel, D. W. Wang, R. E. Dunin-Borkowski, K. W. Urban, and A. Thust, Determination of the 3D shape of a nanoscale crystal with atomic resolution from a single image, Nat. Mater. **13**, 1044 (2014).
[34] R. Xu, H. Jiang, C. Song, J. A. Rodriguez, Z. Huang, C. C. Chen, D. Nam, J. Park, M. Gallagher-Jones, S. Kim, *et al.*, Single-shot three-dimensional structure determination of nanocrystals with femtosecond X-ray free-electron laser pulses, Nat. Commun. **5**, 4061 (2014).
[35] I. Barke, H. Hartmann, D. Rupp, L. Flückiger, M. Sauppe, M. Adolph, S. Schorb, C. Bostedt, R. Treusch, C. Peltz, *et al.*, The 3D-architecture of individual free silver nanoparticles captured by X-ray scattering, Nat. Commun. **6**, 6187 (2015).
[36] C. Zuo, J. Sun, J. Li, A. Asundi, and Q. Chen, Wide-field high-resolution 3D microscopy with Fourier ptychographic diffraction tomography, Opt. Lasers Eng. **128**, 106003 (2020).
[37] T. Latychevskaia, Three-dimensional structure from single two-dimensional diffraction intensity measurement, Phys. Rev. Lett. **127**, 063601 (2021).
[38] A. Colombo, S. Dold, P. Kolb, N. Bernhardt, P. Behrens, J. Correa, S. Düsterer, B. Erk, L. Hecht, A. Heilrath, R. Irsig, *et al.*, Three-dimensional femtosecond snapshots of isolated faceted nanostructures, Sci. Adv. **9**, eade5839 (2023).
[39] A. M. Maiden and J. M. Rodenburg, An improved ptychographical phase retrieval algorithm for diffractive imaging, Ultramicroscopy **109**, 1256 (2009).
[40] P. Thibault and M. Guizar-Sicairos, Maximum-likelihood refinement for coherent diffractive imaging, New J. Phys. **14**, 063004 (2012).
[41] M. J. Humphry, B. Kraus, A. C. Hurst, A. M. Maiden, and J. M. Rodenburg, Ptychographic electron microscopy using high-angle dark-field scattering for sub-nanometre resolution imaging, Nat. Commun. **3**, 730 (2012).
[42] Y. Jiang, Z. Chen, Y. Han, P. Deb, H. Gao, S. Xie, P. Purohit, M. W. Tate, J. Park, S. M. Gruner, *et al.*, Electron ptychography of 2D materials to deep sub-ångström resolution, Nature **559**, 343 (2018).
[43] P. Thibault and A. Menzel, Reconstructing state mixtures from diffraction measurements, Nature **494**, 68 (2013).
[44] S. Cao, P. Kok, P. Li, A. M. Maiden, and J. M. Rodenburg, Modal decomposition of a propagating matter wave via electron ptychography, Phys. Rev. A **94**, 063621 (2016).
[45] Z. Chen, M. Odstrcil, Y. Jiang, Y. Han, M. H. Chiu, L. J. Li, and D. A. Muller, Mixed-state electron ptychography enables sub-angstrom resolution imaging with picometer precision at low dose, Nat. Commun. **11**, 2994 (2020).
[46] J. G. Lozano, G. T. Martinez, L. Jin, P. D. Nellist, and P. G. Bruce, Low-dose aberration-free imaging of Li-rich cathode materials at various states of charge using electron ptychography, Nano Lett. **18**, 6850 (2018).
[47] C. M. O'Leary, G. T. Martinez, E. Liberti, M. J. Humphry, A. I. Kirkland, and P. D. Nellist, Contrast transfer and noise considerations in focused-probe electron ptychography, Ultramicroscopy **221**, 113189 (2021).
[48] H. Sha, Y. Ma, G. Cao, J. Cui, W. Yang, Q. Li, and R. Yu, Sub-nanometer-scale mapping of crystal orientation and depth-dependent structure of dislocation cores in $SrTiO_3$, Nat. Commun. **14**, 162 (2023).
[49] H. Sha, J. Cui, J. Li, Y. Zhang, W. Yang, Y. Li, and R. Yu, Ptychographic measurements of varying size and shape along zeolite channels, Sci. Adv. **9**, eadf1151 (2023).
[50] H. Yang, R. N. Rutte, L. Jones, M. Simson, R. Sagawa, H. Ryll, M. Huth, T. J. Pennycook, M. L. H. Green, H. Soltau, *et al.*, Simultaneous atomic-resolution electron ptychography and Z-contrast imaging of light and heavy elements in complex nanostructures, Nat. Commun. **7**, 12532 (2016).
[51] P. M. Pelz, H. G. Brown, S. Stonemeyer, S. D. Findlay, A. Zettl, P. Ercius, Y. Zhang, J. Ciston, M. C. Scott, and C. Ophus, Phase-contrast imaging of multiply-scattering extended objects at atomic resolution, Phys. Rev. Res. **3**, 023159 (2021).
[52] M. Odstrčil, A. Menzel, and M. Guizar-Sicairos, Iterative least-squares solver for generalized maximum-likelihood ptychography, Opt. Express **26**, 3108 (2018).

[53] K. Wakonig, H. C. Stadler, M. Odstrčil, E. H. R. Tsai, A. Diaz, M. Holler, I. Usov, J. Raabe, A. Menzel, and Manuel Guizar-Sicairos, PtychoShelves, a versatile high-level framework for high-performance analysis of ptychographic data, J. Appl. Crystal. **53**, 574 (2020).

[54] E. H. R. Tsai, I. Usov, A. Diaz, A. Menzel, and M. Guizar-Sicairos, X-ray ptychography with extended depth of field, Opt. Express **24**, 29089 (2016).

[55] Lewys Jones, Absolute Integrator, http://lewysjones.com/software/absolute-integrator/ [Accessed: May 6th, 2020].

[56] J. Miao, D. Sayre, and H. N. Chapman, Phase retrieval from the magnitude of the Fourier transforms of nonperiodic objects, J. Opt. Soc. Am. A **15**, 1662 (1998).

[57] R. Ishikawa, R. Tanaka, S. Morishita, Y. Kohno, H. Sawada, T. Sasaki, M. Ichikawa, M. Hasegawa, N. Shibata, and Yuichi Ikuhara, Automated geometric aberration correction for large-angle illumination STEM, Ultramicroscopy **222**, 113215 (2021).

[58] J. Lee, M. Lee, Y. Park, C. Ophus, and Yongsoo Yang, Multislice electron tomography using four-dimensional scanning transmission electron microscopy, Phys. Rev. Appl. **19**, 054062 (2023).